

Taylor Modeling and Comparative Research Containing Aspect-Ratio Dependent Optimization of Three-Dimensional Hk Superjunction MOSFETs

Zhentaο Xiao^{1,2*}, Haimeng Huang¹, Zonghao Zhang¹, Chenxing Wang^{1,2}

¹University of Electronic Science and Technology of China, Chengdu 610054, China

²University of Glasgow, Glasgow, G12 8QQ, United Kingdom

*Corresponding author: 2839952X@student.gla.ac.uk

Abstract—This paper presents a comprehensive study on aspect-ratio dependent optimization for specific on-resistance of three-dimensional high- k superjunction MOSFETs. The research introduces a Taylor modeling method, overcoming the computational limitations of the Bessel method. It also employs the Chynoweth model for more accurate breakdown voltage determination. The study provides a comparative analysis of four different superjunction structures, across five aspects: electric field, impact ionization integral, aspect ratio dependent optimization, charge imbalance effect and temperature. The findings offer valuable insights for the manufacturing guidance of superjunction structure selection.

Index Terms—Analytic model, Breakdown voltage (BV), Specific ON-resistance ($R_{on,sp}$), Comparative research, Optimization, Taylor series, Three dimensional (3D).

I. INTRODUCTION

In the field of power devices, the breakdown voltage (BV) and the specific on-resistance ($R_{on,sp}$) are the two critical parameters for assessing the quality of a device. However, it has been discovered that BV and $R_{on,sp}$ are interdependent, a constraint known as the ‘Silicon Limit’. The introduction of the Superjunction (SJ) structure has greatly alleviated this constraint [1] [2] [3] [4] [5], allowing devices to achieve higher BV and lower $R_{on,sp}$ through the lateral steering of electric field lines (E-field lines). Due to the charge imbalance and pronounced JFET effect in conventional SJs (C-SJ) [6] [7] [8], the High- k material (Hk) has been proposed to replace the P-pillar to form the high- k superjunction (Hk-SJ) [9] [10] [11] [12]. Beyond this, driven by the need for process optimization and further performance enhancement, both Hk-SJs and C-SJs are evolving towards a three dimensional (3D) direction [6] [7] [8] [9] [13]. However, compared to the research on 3D C-SJs, the research on 3D Hk-SJs is scarce and not in-depth. Generally speaking, the 3D Hk-SJ is divided into two categories [9], as shown in Fig. 1(a) and (b), namely 3DHkcase1 and 3DHkcase2, which differ in the position of the Hk layer and the lateral steering of E-field are also shown.

Through literature review, the cutting-edge 3D Hk-SJ research still has the following shortcomings: 1. The E-field modeling of 3D Hk-SJs is limited to the Bessel method [9], which is computationally intensive and time-consuming. 2. The optimization of 3D Hk-SJs is not comprehensive, with

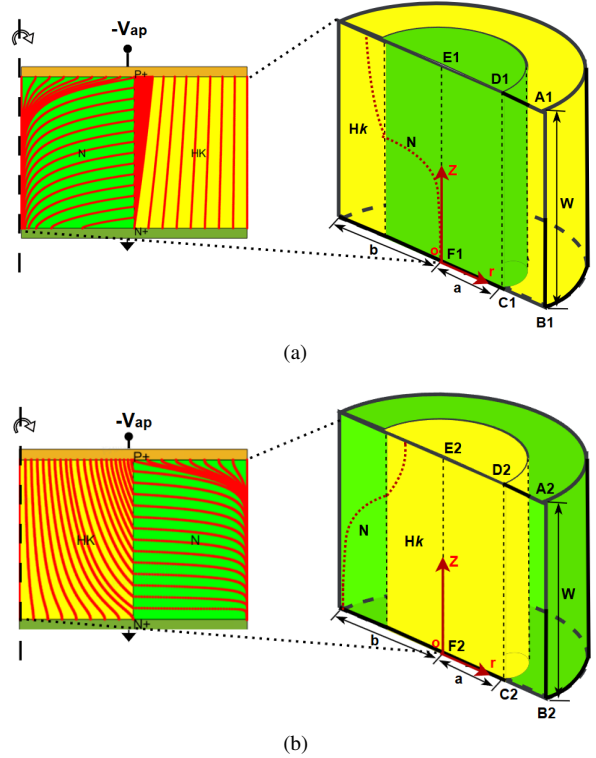


Fig. 1. Structure and E-field lines of (a) 3DHkcase1 and (b) 3DHkcase2. The E-field lines are calculated and drawn by MATLAB using the methodology in [11].

no optimization dependent on the aspect ratio. 3. Only the Fulop impact ionization integral model is used [9], with no application of the Chynoweth precise model, leading to inaccurate BV [6]. 4. The research on 3D Hk-SJs is relatively isolated, with no comparative studies between 2D Hk-SJs (2DHk) and different types of 3D Hk-SJs, resulting in poor manufacturing guidance.

Considering the aforementioned reasons, this article proposes a Taylor modeling method for 3DHkcase2 in Section II and uses the Taylor method and Chynoweth model to complete the aspect ratio dependent optimization. Section III will consider a comprehensive comparison and analysis of the advantages and disadvantages of 3D C-SJ, 2DHk, 3DHkcase1,

and 3DHkcase2, comparing from five aspects: E-field, impact ionization integral, aspect ratio dependent optimization, charge imbalance, and temperature. Finally, in Section IV, we will place the 3D Hk-SJ structure within MOSFETs and complete a comparative analysis of electrical characteristics. Section V will summarize the entire article.

II. ANALYTIC E-FIELD MODELING OF 3DHk-SJ

A. Error Correction of Bessel Method

Before presenting the Taylor modeling approach, we first correct the error in the potential distribution expression (V_{Hk}) in the Hk region of 3DHkcase2 from [9]. First, the Poisson equation in 3D cylindrical coordinates is given by

$$\begin{cases} \nabla^2 V_S(r, z, \theta) = -\frac{qN}{\epsilon_S}, \\ \nabla^2 V_{Hk}(r, z, \theta) = 0. \end{cases} \quad (1)$$

The equations above can be expanded and simplified as follows due to the symmetry,

$$\begin{cases} \frac{\partial^2 V_S}{\partial r^2} + \left(\frac{\partial V_S}{\partial r}\right)\frac{1}{r} + \frac{\partial^2 V_S}{\partial z^2} = -\frac{qN}{\epsilon_S}, \\ \frac{\partial^2 V_{Hk}}{\partial r^2} + \left(\frac{\partial V_{Hk}}{\partial r}\right)\frac{1}{r} + \frac{\partial^2 V_{Hk}}{\partial z^2} = 0. \end{cases} \quad (2)$$

For 3DHkcase2, the boundary conditions can be written as

$$\begin{cases} V_S(z=0) = V_{Hk}(z=0) = 0, \\ V_S(z=W) = V_{Hk}(z=W) = -V_{ap}, \\ \epsilon_S \frac{\partial V_S}{\partial r}\Big|_{r=a} = \epsilon_{Hk} \frac{\partial V_{Hk}}{\partial r}\Big|_{r=a}, \\ V_S(r=a) = V_{Hk}(r=a), \\ \frac{\partial V_S}{\partial r}\Big|_{r=b} = \frac{\partial V_{Hk}}{\partial r}\Big|_{r=0} = 0, \end{cases} \quad (3)$$

where, V_{ap} means the applied voltage as shown in Fig.1. Finally, we can solve the potential distribution of Hk region from equations (2) and (3):

$$V_{Hk} = -\frac{V_{ap}}{W}z + \frac{4NW^2q}{\pi^3\epsilon_{Hk}} \sum_{n=\text{odd}} \frac{I_0\left(\frac{n\pi r}{W}\right) \sin\left(\frac{n\pi z}{W}\right)}{n^3 \left[\frac{\epsilon_S}{\epsilon_{Hk}} I_0\left(\frac{n\pi a}{W}\right) - \frac{\beta_n}{\alpha_n} I_1\left(\frac{n\pi a}{W}\right) \right]} \quad (4)$$

where, $\alpha_n = I_1\left(\frac{n\pi a}{W}\right)K_1\left(\frac{n\pi b}{W}\right) - I_1\left(\frac{n\pi b}{W}\right)K_1\left(\frac{n\pi a}{W}\right)$ and $\beta_n = I_0\left(\frac{n\pi a}{W}\right)K_1\left(\frac{n\pi b}{W}\right) + I_1\left(\frac{n\pi b}{W}\right)K_0\left(\frac{n\pi a}{W}\right)$, respectively. Fig. 2(a) shows a comparison between the results calculated from equation (4) and the MEDICI (TCAD software) simulation results. The excellent agreement between the two confirms the accuracy of equation (4).

B. E-Field's Taylor Method Modeling

For the Taylor modeling method, we also use equation (2) and the boundary conditions in equation (3). Additionally, we perform a Taylor expansion of $V_S(r, z)$ and $V_{Hk}(r, z)$ at $r = b$ and $r = 0$, respectively, retaining only the first three terms of the expansion. They are found as:

$$\begin{cases} V_S(r, z) = V_S(b, z) + \frac{\partial V_S(b, z)}{\partial r}\Big|_{r=b} \cdot (r-b) \\ \quad + \frac{\partial^2 V_S(b, z)}{\partial r^2}\Big|_{r=b} \cdot \frac{(r-b)^2}{2}, \\ V_{Hk}(r, z) = V_{Hk}(0, z) + \frac{\partial V_{Hk}(0, z)}{\partial r}\Big|_{r=0} \cdot r \\ \quad + \frac{\partial^2 V_{Hk}(0, z)}{\partial r^2}\Big|_{r=0} \cdot \frac{r^2}{2}. \end{cases} \quad (5)$$

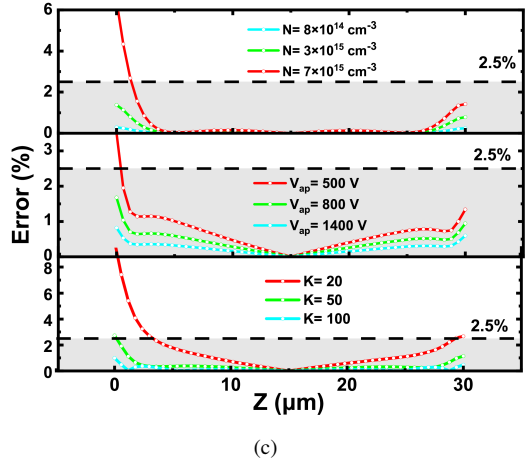
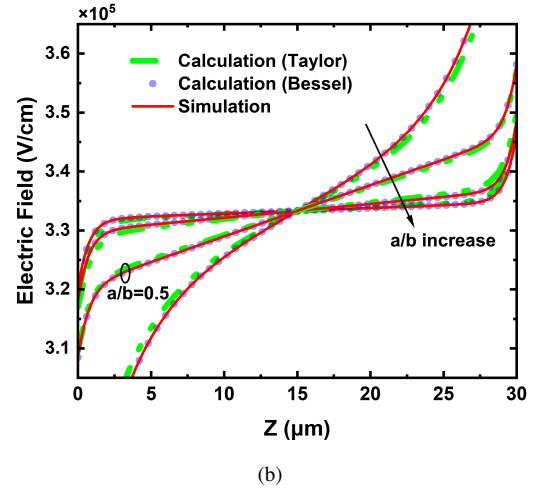
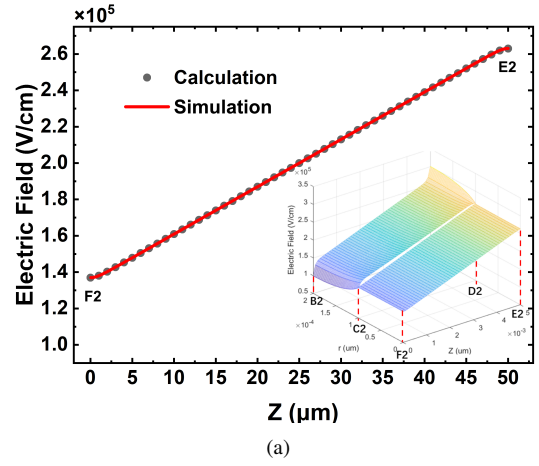


Fig. 2. (a) The comparison between the calculation using equation (4) and simulation result along F_2E_2 , with 3D depiction of entire E-field distribution under same condition. (b) The comparison between Bessel [9], Taylor method and simulation along A_2B_2 at $r = b$ under different a/b . (c) The error of Taylor method along A_2B_2 at $r = b$ under different conditions. Error = $\text{abs}(100\% \times [E(\text{Taylor}) - E(\text{Bessel})]/E(\text{Bessel}))$.

Then, through the calculation, $V_S(b, z)$ can be found as

$$V_S(b, z) = \left(\frac{2}{\lambda^2 T_d^2} - 1 + \frac{b^2}{2T_d^2} \right) [A \exp(\lambda z) + B \exp(-\lambda z)] - \frac{T_e^2}{T_d^2} \frac{qN}{\epsilon_S} z^2 + Dz + E, \quad (6)$$

where T_c , T_d , and T_e are dimensioned constants with units of μm , $T_c^2 = -\frac{1}{2} \left[\frac{\epsilon_S}{\epsilon_{HK}} a(a-b) - 1.42(a-b)^2 \right]$, $T_d^2 = \frac{1}{2} \left[a^2 - \frac{\epsilon_S}{\epsilon_{HK}} a(a-b) \right]$, and $\frac{1}{T_e^2} = \frac{2}{T_d^2} + \frac{1}{T_c^2}$. Above three are structural constants which only depend on the structure parameters such as a and b . λ is the root of characteristic equation of differential equation during the calculation and $\lambda = \left(T_e \cdot \sqrt{1 - (b/T_d)^2} / 2 \right)^{-1}$. The coefficients A , B , D and E are found as

$$\begin{cases} A = \frac{T_e^2 qN / \epsilon_S}{\exp(W\lambda) + 1}, \\ B = \frac{T_e^2 qN / \epsilon_S \cdot \exp(W\lambda)}{\exp(W\lambda) + 1}, \\ D = -\frac{T_d^2 V_{ap} - T_e^2 qNW^2 / \epsilon_S}{T_d^2 W}, \\ E = -\frac{T_e^2 qN / \epsilon_S \cdot (-2T_d^2 \lambda^2 + b^2 \lambda^2 + 4)}{2T_d^2 \lambda^2}. \end{cases} \quad (7)$$

The distribution of the electric field at $r = b$ is derived by differentiating equation (6) and is given as

$$E_S(b, z) = - \left(\frac{2}{\lambda^2 T_d^2} - 1 + \frac{b^2}{2T_d^2} \right) [A\lambda \exp(\lambda z) - B\lambda \exp(-\lambda z)] + 2 \frac{T_e^2 qN}{T_d^2 \epsilon_S} z - D. \quad (8)$$

In fact, we only need to know the expressions for the potential and E-field at $r = b$, and we do not need to know the complete expressions for V_s and V_{HK} . This is because, as stated in [9] and verified through simulations, avalanche breakdown occurs first along the E-field line from A_2 to B_2 .

Fig. 2(b) shows a comparison of the E-field along A_2B_2 for different a/b values. The results obtained using the Taylor method, the Bessel method [9] and simulation demonstrate good consistency with each other. The error of Taylor method is depicted in Fig. 2(c) which indicates that with different doping concentration (N), V_{ap} and K ($K = \epsilon_S / \epsilon_{HK}$), the error along the z -direction at $r = b$ mainly less than 2.5%. The error at $z = 0$ is relatively large, but this does not affect the accuracy of subsequent calculations because $z = 0$ corresponds to the point where the E-field reaches its minimum value (as shown in Fig. 2(b)). Since the E-field is minimal at this location, it does not influence the accuracy of the subsequent impact ionization integral calculation.

C. Aspect Ratio Dependent Optimization using Taylor Method

For superjunction devices, there are many optimization methods available. Unlike in [9], here we select the critical depletion and critical breakdown as two constraints. Following the methodology outlined in [10], we can perform an $R_{on,sp}$ optimization that depends on the aspect ratio (AR_S , $AR_S =$

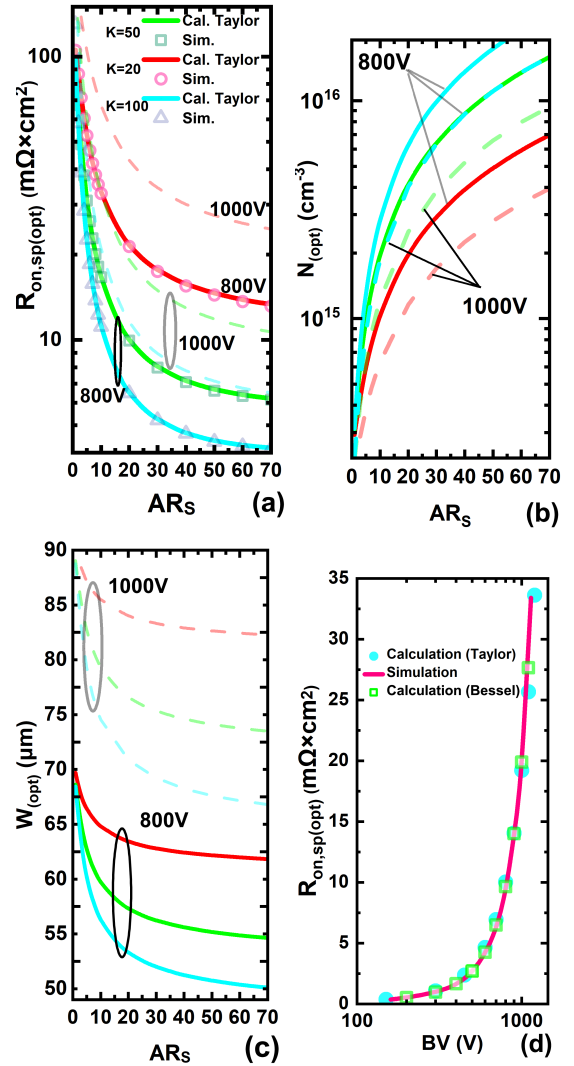


Fig. 3. Aspect ratio dependent optimization results (Taylor method) of (a) $R_{on,sp}$, (b) N and (c) W under the condition of 3DHCcase2 with $a=2 \mu\text{m}$ and K varies from 20 to 100. (d) $R_{on,sp}$ - BV curve used for optimization accuracy confirmation.

$W / [2 \times (\text{Width of } N \text{ region})]$). $R_{on,sp}$ for two cases can be determined as

$$R_{on,sp} = \begin{cases} \frac{W}{q\mu_n N} \cdot \frac{b^2}{a^2}, & \text{for 3DHCcase1,} \\ \frac{W}{q\mu_n N} \cdot \frac{b^2}{b^2 - a^2}, & \text{for 3DHCcase2.} \end{cases} \quad (9)$$

The breakdown conditions can be determined through the calculation of impact ionization integral. The Chynoweth model [14] is applied for higher accuracy of confirming breakdown,

$$I_n = \int \alpha_n \exp \left(\int^s (\alpha_p - \alpha_n) ds' \right) ds. \quad (10)$$

Using the methodology from [10] and MATLAB calculations, the optimization results for $R_{on,sp(opt)}$, $N_{(opt)}$ and $W_{(opt)}$ are presented in Fig. 3(a), (b) and (c), respectively, for given values of BV (800 V and 1000 V). From the three figures, it can be observed that under the two constraints mentioned

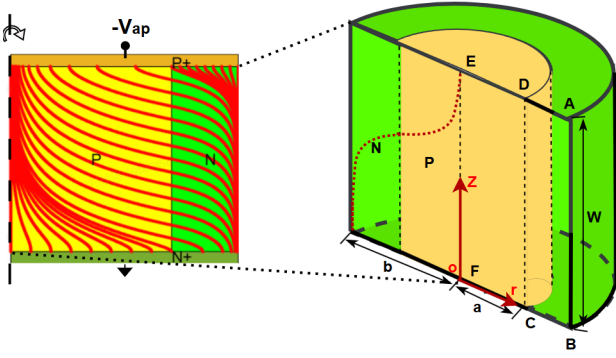


Fig. 4. Structure and E-field lines of 3D C-SJ. The E-field lines are calculated and drawn by MATLAB using the methodology in [11].

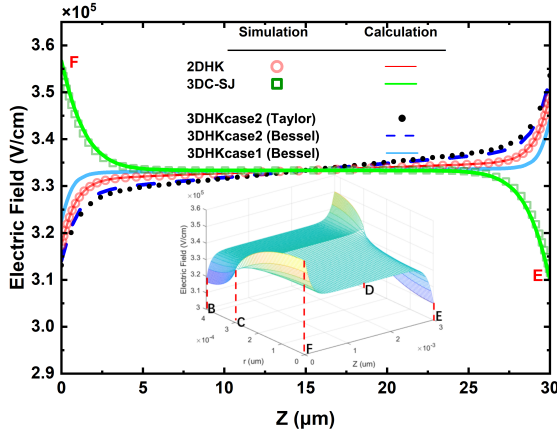


Fig. 5. E-field comparison of 4 structures along breakdown path (E_1F_1 for 3DHkcase1 and 2Dhk, A_2B_2 for 3DHkcase2, EF for 3D C-SJ), with 3D depiction of entire E-field of 3D C-SJ.

before and given BV, as AR_S increases, the doping concentration $N_{(opt)}$ gradually increases while the device height $W_{(opt)}$ decreases, resulting in a reduction in $R_{on,sp (opt)}$. This implies that, in the manufacturing process, one can achieve a lower $R_{on,sp (opt)}$ by increasing the AR_S (or, say, reducing the width of the N-region). Additionally, using high dielectric constant materials as high- k material and reducing the BV can further reduce $R_{on,sp (opt)}$. Specifically, the minimum value, $4.156 m\Omega \cdot cm^2$, can be achieved when $BV = 800$ V, $K = 100$, $AR_S = 70$, $W_{(opt)} = 50.093 \mu m$ and $N_{(opt)} = 2.49 \times 10^{16} cm^{-3}$. Fig. 3(d) shows the relationship between $R_{on,sp (opt)}$ and BV through Taylor method, Bessel method and simulation. The consistency of the three results indicates the high accuracy of above optimization using Taylor method.

III. COMPREHENSIVE COMPARATIVE ANALYSIS OF 3DHk-SJ

Before the comparative analysis, the structure and E-field lines of 3D C-SJ is introduced in Fig. 4. The structure of 2Dhk is the same as the profile of 3DHkcase1. For 3D C-SJ, $AR_S = W / [2 \times (\text{Width of P region})]$ and ensure charge neutrality for 3D C-SJ in all subsequent discussions.

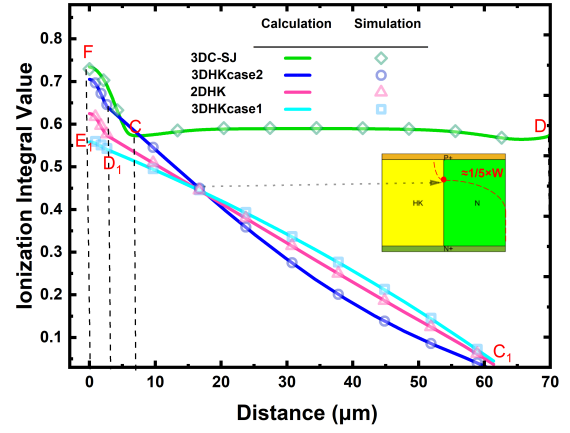


Fig. 6. Simulation and calculation results of impact ionization integral values along $E_1D_1C_1$ for 3DHkcase1 and 2Dhk, $A_2D_2C_2$ for 3DHkcase2 and FCD for 3D C-SJ.

A. Breakdown E-field Comparative Analysis

With all the parameters set to: $V_{ap} = 1000$ V, $W = 30 \mu m$, the width of the N region is $1.243 \mu m$, the width of the P region (Hk region) is $3 \mu m$, $K = 50$, $N = 1 \times 10^{15} cm^{-3}$, the E-field along the breakdown path for each structure under same condition are shown in Fig. 5. It is obvious that, from the figure, 3D C-SJ has the highest peak E-field and 3DHkcase1 has the lowest, suggesting that the 3D C-SJ is more prone to breakdown under the same conditions, while the 3DHkcase1 is less likely to break down under the same conditions.

B. Ionization Integral Comparative Analysis

To further determine the breakdown characteristics of these structures, the calculation and comparison of the impact ionization integral are necessary. Using equation (10) and methodology in [11] with parameters set as follows [6]: $W = 63.3 \mu m$, the width of the P region (Hk region) = $6.33 \mu m$, the width of the N region = $2.62 \mu m$, $N = 1.97 \times 10^{15} cm^{-3}$, $V_{ap} = 900$ V, $K = 50$. The values of the impact ionization integral along specific paths are shown in Fig. 6. From the figure, it can be seen that consistent with the conclusion of Fig. 5, the 3D C-SJ has the largest impact ionization integral value at point F, meaning it is more likely to occur avalanche break down under the same conditions, while the 3DHkcase1 is the least likely to occur.

C. Aspect Ratio Optimization Comparative Analysis

The optimization trends of the four structures are shown in Fig. 7(a), (b), and (c). The optimized design parameters acquired from Fig. 7(a) are shown in TABLE I. For the 3DHkcase2, the optimization results and trends are similar to those in Fig. 3. Additionally, the optimization results of the Taylor method and the Bessel method exhibit a high degree of consistency. It can be observed from Fig. 7(a) and TABLE I that, except for the 3DHkcase2, the remaining three structures all have a minimum value for $R_{on,sp (opt)}$. For the 3DHkcase1, the minimum value (12.427) is achieved at a small AR_S , and its minimum value is higher than that of

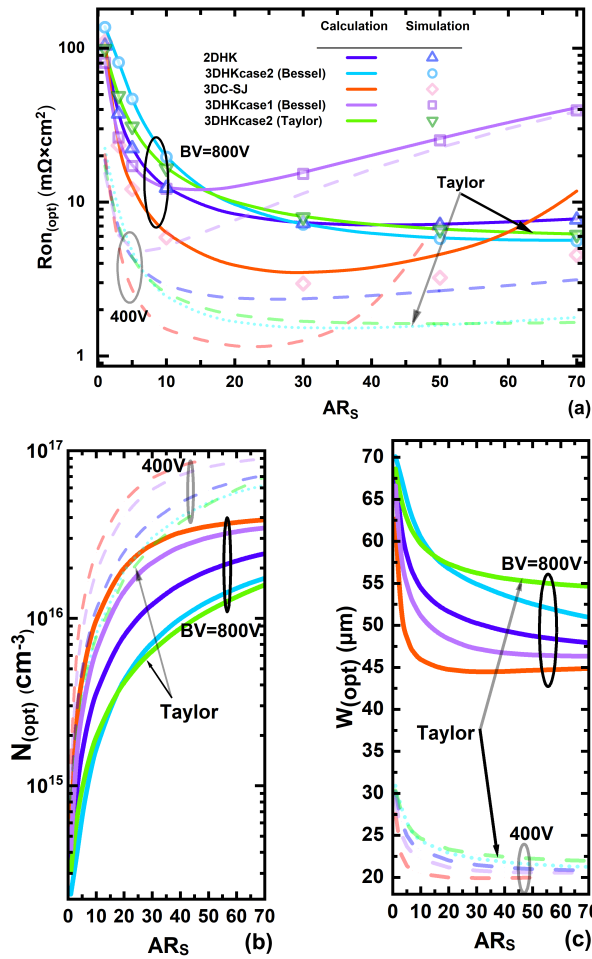


Fig. 7. Aspect ratio dependent optimization results for the 4 structures (containing Taylor method) of (a) $R_{on,sp}$, (b) N and (c) W under the condition of Hk region width = $2 \mu\text{m}$, $K=50$, $BV=400 \text{ V}$ and 800 V .

3D C-SJ, 2DHk and 3DHkcase2 by 72%, 43% and 55%, implying that the 3DHkcase1 structure is challenging to reduce $R_{on,sp(opt)}$ under the given BV. It is noteworthy that the 3D C-SJ can optimize a smallest $R_{on,sp(opt)}$ (3.488) at a larger AR_s compared to the other structures, which means that the 3D C-SJ can achieve a more favorable $R_{on,sp(opt)}$ under the given BV compared to other structures. For the 2DHk, the minimum value is relatively less pronounced, however, its smallest $R_{on,sp(opt)}$ (7.104) lies between that of the 3DHkcase2

TABLE I

OPTIMIZATION RESULTS OF 3D C-SJ, 2DHk, 3DHkCASE1, AND 3DHkCASE2 AT $BV = 800 \text{ V}$, Hk REGION WIDTH = $2 \mu\text{m}$ AND $K = 50$

Symbol	3D C-SJ	2DHk	3DHkcase1	3DHkcase2	Unit
$N_{(opt)}$	2.75×10^{16}	1.59×10^{16}	6.41×10^{15}	1.73×10^{16}	cm^{-3}
$W_{(opt)}$	44.481	49.357	51.137	50.935	μm
a	0.741	0.617	2.557	2	μm
b	1.048	2.617	4.557	2.364	μm
$R_{on,sp(opt)}$	3.488	7.104	12.427	5.653	$\text{m}\Omega \cdot \text{cm}^2$

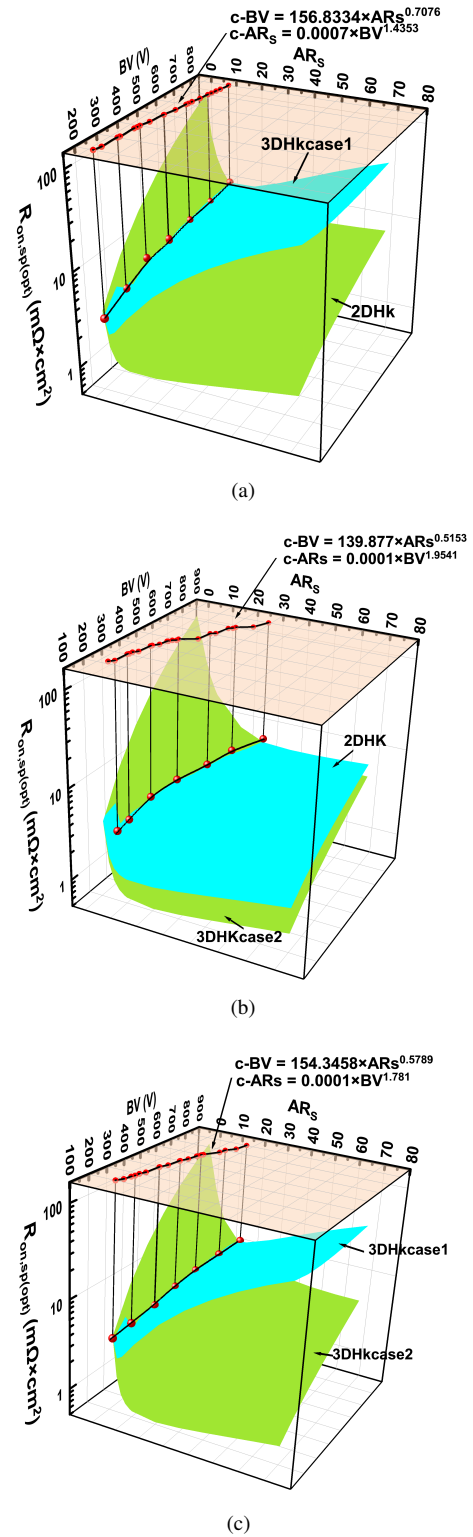


Fig. 8. Boundary curves with same $R_{on,sp(opt)}$ for (a) 3DHkcase1 and 2DHk, (b) 2DHk and 3DHkcase2, (c) 3DHkcase1 and 3DHkcase2, along with their boundary curves' expressions.

(5.653) and the 3DHkcase1 (12.427). The minimum $R_{on,sp(opt)}$ for the 3DHkcase2 is still achieved at the maximum AR_s , with its smallest $R_{on,sp(opt)}$ (5.653) achieve 120% and 26% better

than that of the 3DHkcase1 and 2DHk, but 38% worse than that of 3D C-SJ.

Fig. 8(a), (b), and (c) present 3D plots of $R_{on,sp(opt)}$ as a function of AR_S and BV, from which we can derive guidance for production and manufacturing. Taking Fig. 8(a) as an example, for larger AR_S and smaller BV, 2DHk can achieve a smaller $R_{on,sp(opt)}$, while for smaller AR_S and larger BV, 3DHkcase1 can achieve a smaller $R_{on,sp(opt)}$. Quantitatively speaking, if the AR_S that can be achieved in device production is determined, the critical BV (c-BV) can be obtained through the boundary curve formula shown in Fig. 8(a). If a device which requires a BV greater than the c-BV needs to be produced, 3DHkcase1 is the better choice because of lower $R_{on,sp(opt)}$. If the BV of the device is determined, the critical AR_S (c- AR_S) can be obtained through the boundary curve formula. If the production process supports the creation of a large AR_S , i.e., $AR_S > c-AR_S$, 2DHk is the better choice. The same principle applies to Fig. 8(b) and (c). By using the formulas of the boundary curves, we can compare the advantages and disadvantages of 2DHk, 3DHkcase1 and 3DHkcase2 under given conditions, thereby providing valuable guidance for the production of 3D Hk-SJ devices.

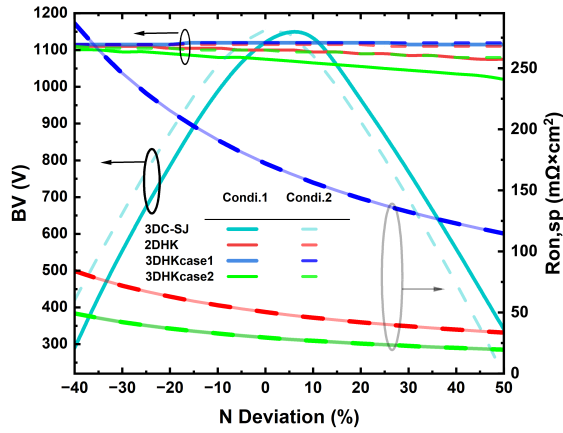


Fig. 9. Charge imbalance effect of BV and $R_{on,sp(opt)}$ as a function of deviation of N for the four different structures at condition 1 and 2.

D. Charge Imbalance Comparative Analysis

Fig. 9 illustrates the degradation of BV and $R_{on,sp(opt)}$ due to the error in N. The structural parameter settings are divided into two conditions. The first condition (solid lines) is consistent with Fig. 6, while the second condition (dashed lines) modifies the width of the P region (Hk region) to 3.3 μm and the width of the N region to 1.367 μm based on the first condition. It can be observed from the Fig. 9 that regardless of the structure parameters, the sensitivity of BV to errors in all high-k superjunction structures is far less than that of the 3D C-SJ. This implies that the use of various high-k superjunction structures can significantly enhance the robustness of BV against N errors. Regarding $R_{on,sp(opt)}$, all Hk-SJs are noticeably affected by errors, but 3DHkcase1 is more sensitive to errors compared to 2DHk and 3DHkcase2.

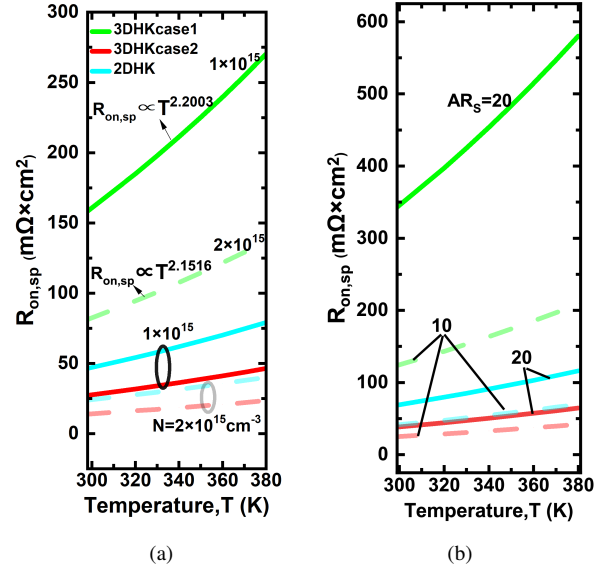


Fig. 10. $R_{on,sp}$ as a function of temperature for three 3D Hk-SJ structures at (a) different N and (b) different AR_S .

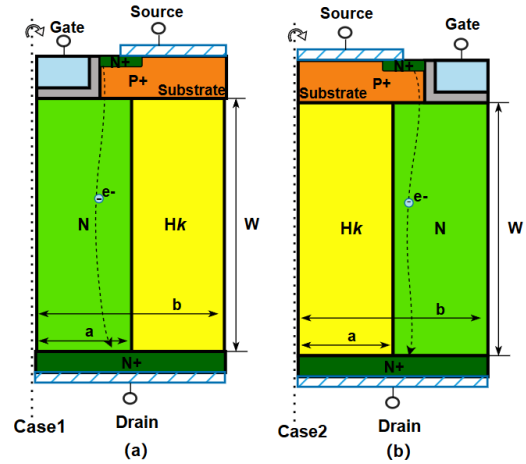


Fig. 11. The cross-section structures of (a) 3DHkcase1 and (b) 3DHkcase2 MOSFETs. 2DHk MOSFET shares the same structure of 3DHkcase1.

E. Temperature characteristic Comparative Analysis

Fig. 10(a) and (b) depict the temperature dependence of $R_{on,sp(opt)}$ for three 3D Hk-SJ structures under varying N and different AR_S . From Fig. 10(a), it is evident that 3DHkcase1's $R_{on,sp(opt)}$ is the most sensitive to temperature, while the $R_{on,sp(opt)}$ of 3DHkcase2 and 2DHk exhibit similar robustness against temperature variations. This implies that if the device is expected to operate under high-temperature conditions, 3DHkcase2 and 2DHk are the better choices. Additionally, appropriately increasing the N can reduce the temperature sensitivity of 3DHkcase1. As shown in Fig. 10(a), a higher doping concentration will decrease the exponent of T from 2.2003 to 2.1516.

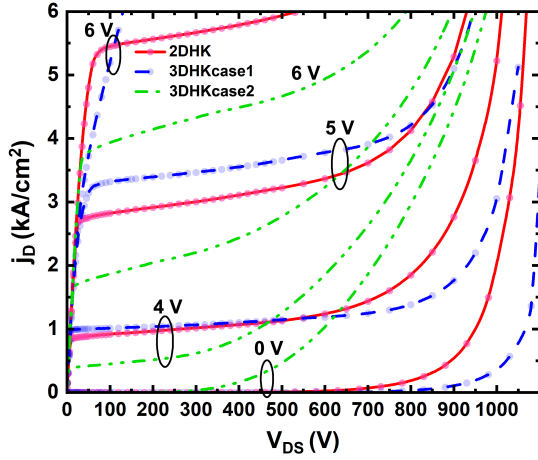


Fig. 12. Output characteristic of three 3D Hk-SJ MOSFETs by simulation results at different V_{GS} .

IV. ELECTRICAL CHARACTERISTIC ANALYSIS OF DIFFERENT Hk-SJ MOSFETs

The cross-sectional views of the structures for 3DHkcase1 and 3DHkcase2 MOSFETs are shown in Fig. 11(a) and (b), respectively, with the meanings of the structural parameters being consistent with Fig. 1. Here, $W=75 \mu\text{m}$, $N=5 \times 10^{15} \text{cm}^{-3}$, N region width= $2 \mu\text{m}$, Hk region width= $6 \mu\text{m}$, $K=20$, and the doping concentrations for the Drain region, Substrate, and Source region are 1×10^{19} , 2×10^{17} , and $3 \times 10^{19} \text{cm}^{-3}$, respectively. The channel length is approximately $4 \mu\text{m}$, and the gate oxide thickness is 35nm . CONSRH, AUGER, ANALYTIC, FLDMOB, BGN, INCOMPLE and IMPACT.I are used as physical models in MEDICI simulation.

A. Static Output Characteristic

Fig. 12 demonstrates the static output characteristics and breakdown behavior of three different Hk-SJ MOSFETs, where j_D is the current density of the drain and V_{DS} is the applied voltage across the drain and source. As shown in Fig. 5 and Fig. 6, 3DHkcase1, with its smaller peak breakdown electric field and impact ionization integral value, is the most difficult one to break down among the three structures at $V_{GS} = 0 \text{V}$, followed by 2DHk, while 3DHkcase2 is the easiest one to break down.

B. Switching Responses Characteristic

Fig. 13(a) and (b) display the switching responses of the three structures. Here, V_{GS} is ramped up from 0V to 4V (and down from 4V to 0V) within 0.1ns , while V_{dd} is maintained at 200V . From Fig. 13(a), it can be observed that 2DHk turns on the fastest, followed by 3DHkcase1, and then 3DHkcase2. From Fig. 13(b), it is evident that 3DHkcase2 turns off the quickest, followed by 2DHk, and then 3DHkcase1. This implies that 3DHkcase1 has relatively poor switching characteristics, while 3DHkcase2 is suitable for applications in fast chopper circuits.

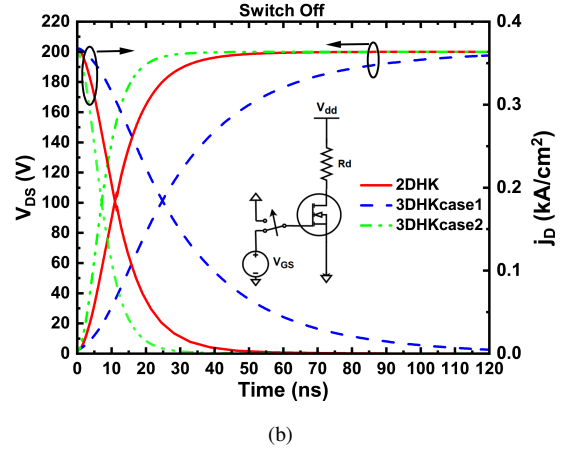
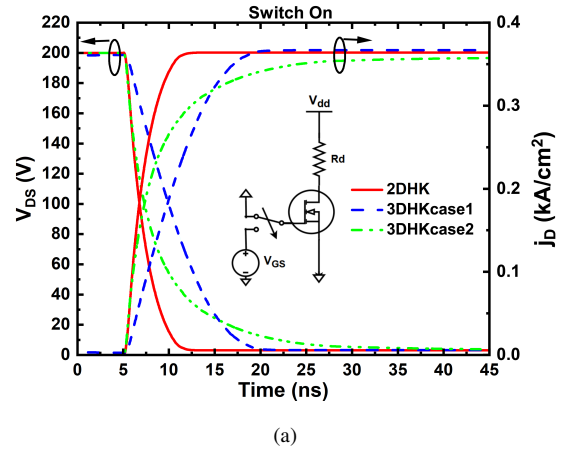


Fig. 13. Switching responses of three 3D Hk-SJ MOSFETs by simulation results. (a) Switch-on. (b) Switch-off

V. CONCLUSION

In summary, this article proposes a Taylor modeling method for 3DHkcase2 and achieve $R_{on,sp(opt)}$ optimization to $4.156 \text{m}\Omega \cdot \text{cm}^2$ at $BV = 800 \text{V}$ and $K = 100$. Through comparative analysis under the same conditions among 3D C-SJ, 2DHk, 3DHkcase1 and 3DHkcase2, we find that 3D C-SJ has the potential to optimize for the smallest $R_{on,sp}$ to $3.488 \text{m}\Omega \cdot \text{cm}^2$ at $BV = 800 \text{V}$ but is the worst at resisting N deviation. 3DHkcase1 can have a larger BV compared to 3DHkcase2 and 2DHk, but the $R_{on,sp(opt)}$ of 3DHkcase2 after optimization can be 120%, 26% smaller than that of 3DHkcase1 and 2DHk, and case2 also outperforms case1 in terms of switching characteristics and temperature robustness. The performance of 2DHk is usually between case1 and case2. Furthermore, through the formulas of boundary curves, we can provide effective guidance for structure selection in superjunction device manufacturing.

REFERENCES

- [1] X.-B. Chen and J. Sin, "Optimization of the specific on-resistance of the coolmos/sup tm/," *IEEE Transactions on Electron Devices*, vol. 48, no. 2, pp. 344–348, 2001.

- [2] H. Ye and P. Haldar, "Optimization of the porous-silicon-based superjunction power mosfet," *IEEE Transactions on Electron Devices*, vol. 55, no. 8, pp. 2246–2251, 2008.
- [3] A. Strollo and E. Napoli, "Optimal on-resistance versus breakdown voltage tradeoff in superjunction power devices: a novel analytical model," *IEEE Transactions on Electron Devices*, vol. 48, no. 9, pp. 2161–2167, 2001.
- [4] X. Chen, P. Mawby, K. Board, and C. Salama, "Theory of a novel voltage-sustaining layer for power devices," *Microelectronics Journal*, vol. 29, no. 6, pp. 1005–1011, 1998.
- [5] X.-B. Chen, H.-Q. Yang, and M. Cheng, "New "silicon limit" of power devices," *Solid-State Electronics*, vol. 46, no. 9, pp. 1185–1192, 2002.
- [6] H. Huang, Y. Xu, H. Li, Z. Zhang, Y. Li, H. Zhang, J. Cheng, B. Yi, Z. Wang, and G. Zhang, "Optimization and comparison of specific on-resistance for superjunction mosfets considering three-dimensional and insulator-pillar concepts," *IEEE Transactions on Electron Devices*, vol. 69, no. 3, pp. 1162–1168, 2022.
- [7] H. Kang and F. Udrea, "Theory of 3-d superjunction mosfet," *IEEE Transactions on Electron Devices*, vol. 66, no. 12, pp. 5254–5259, 2019.
- [8] W. Zhang, K. Zhang, L. Wu, Y. Sun, X. Guo, Z. Wang, M. Qiao, Z. Li, and B. Zhang, "The minimum specific on-resistance of 3-d superjunction devices," *IEEE Transactions on Electron Devices*, vol. 70, no. 3, pp. 1206–1210, 2023.
- [9] X. Lyu and X. Chen, "Vertical power hk-mosfet of hexagonal layout," *IEEE Transactions on Electron Devices*, vol. 60, no. 5, pp. 1709–1715, 2013.
- [10] H. Huang, S. Xu, W. Xu, K. Hu, J. Cheng, H. Hu, and B. Yi, "Optimization and comparison of drift region specific on-resistance for vertical power hk mosfets and sj mosfets with identical aspect ratio," *IEEE Transactions on Electron Devices*, vol. 67, no. 6, pp. 2463–2470, 2020.
- [11] H. Huang, K. Hu, W. Xu, S. Xu, W. Cui, W. Zhang, and W. T. Ng, "Numerical solutions for electric field lines and breakdown voltages in superjunction-like power devices," *IEEE Transactions on Electron Devices*, vol. 67, no. 9, pp. 3898–3902, 2020.
- [12] Z. Wang, X. Wang, and J. B. Kuo, "Modeling power vertical high-k mos device with interface charges via superposition methodology-breakdown voltage and specific on-resistance," *IEEE Transactions on Electron Devices*, vol. 65, no. 11, pp. 4947–4954, 2018.
- [13] J. Park and J.-H. Lee, "A 650 v super-junction mosfet with novel hexagonal structure for superior static performance and high by resilience to charge imbalance: A tcad simulation study," *IEEE Electron Device Letters*, vol. 38, no. 1, pp. 111–114, 2017.
- [14] A. G. Chynoweth, "Ionization rates for electrons and holes in silicon," *Physical Review*, vol. 109, no. 5, p. 1537, May 1958.